CHAOS IN THE TEST PARTICLE ECCENTRIC KOZAI–LIDOV MECHANISM

GONGJIE LI, SMADAR NAOZ, MATT HOLMAN, AND ABRAHAM LOEB
Harvard-Smithsonian Center for Astrophysics, The Institute for Theory and Computation, 60 Garden Street,
Cambridge, MA 02138, USA; gli@cfa.harvard.edu

ABSTRACT

The Kozai–Lidov mechanism can be applied to a vast variety of astrophysical systems involving hierarchical three-body systems. Here, we study the Kozai–Lidov mechanism systematically in the test particle limit at the octupole level of approximation. We investigate the chaotic and quasi-periodic orbital evolution by studying the surfaces of section and the Lyapunov exponents. We find that the resonances introduced by the octupole level of approximation cause orbits to flip from prograde to retrograde and back as well as cause significant eccentricity excitation, and chaotic behavior occurs when the mutual inclination between the inner and the outer binary is high. We characterize the parameter space that allows large amplitude oscillations in eccentricity and inclination.

Key words: binaries: close – celestial mechanics

Online-only material: color figures

1. INTRODUCTION

The Kozai–Lidov mechanism (Kozai 1962; Lidov 1962) has proven very useful for interpreting numerous astrophysical systems. For example, it has been shown that it can play a major role in exoplanet configurations and obliquities (e.g., Holman et al. 1997; Wu & Murray 2003; Fabrycky & Tremaine 2007; Veras & Ford 2010; Correia et al. 2011; Naoz et al. 2011, 2012). In addition, close stellar binaries with two compact objects are likely produced through triple evolution, and the Kozai–Lidov mechanism may play a key role in these systems (e.g., Harrington 1969; Mazeh & Shaham 1979; Soderhjelm 1982; Kiseleva et al. 1998; Ford et al. 2000; Eggleton & Kiseleva-Eggleton 2001; Fabrycky & Tremaine 2007; Perets & Fabrycky 2009; Thompson 2011; Katz & Dong 2012; Shappee & Thompson 2013; Naoz et al. 2013; Naoz & Fabrycky 2014). Furthermore, the Kozai–Lidov mechanism has been proposed as an important element in the growth of black holes at the centers of dense star clusters, the formation of short-period binary black holes (Blaes et al. 2002; Miller & Hamilton 2002; Wen 2003; Ivanova et al. 2010), and tidal disruption events (Chen et al. 2009, 2011; Wegg & Bode 2011; Bode & Wegg 2013; G. Li et al., in preparation).

The Kozai–Lidov mechanism focuses on hierarchical three-body systems, which can be treated as the interaction between two elliptical wires by orbit averaging: the inner wire is composed of the inner two objects, and the outer wire is composed of the outer companion orbiting around the center of mass of the inner two objects. The total angular momentum of this system, the vector sum of the inner orbit's and the outer orbit's angular momenta, is conserved.

Kozai (1962) and Lidov (1962) first studied this mechanism by expanding the gravitational potential in a power series of the semi-major axis ratio and considered applications when one of the inner objects is massless (the test particle limit) and the outer orbit is circular. Kozai (1962) considered the secular (long-term) evolution of asteroids under the perturbation of Jupiter, and Lidov (1962) studied the secular evolution of satellites under the perturbation of the Moon. In those cases, the gravitational potential of the inner orbit is axisymmetric, which renders the $\hat{z}$ component of the inner orbit's angular momentum (J_z) constant, where $\hat{z}$ is the direction of the total angular momentum of the

system. The quadrupole order of approximation ($O((a_1/a_2)^2)$) sufficiently describes the orbital evolution of such systems, and the eccentricity and the inclination undergo large amplitude oscillations due to the "Kozai resonance" when $i > 39°.2$.

Recently, Naoz et al. (2011) considered the case when none of the inner objects is a test particle, and pointed out that J_z is no longer conserved. In addition, the eccentric Kozai–Lidov mechanism (hereafter EKL) applies to cases when the outer orbit is non-circular, where the $\hat{z}$ component of the angular momentum of the inner orbit is also not conserved (Naoz et al. 2011). In this situation, the octupole terms in the potential ($O((a_1/a_2)^3)$) need to be taken into account to describe the orbital evolution, where the eccentricity of the inner orbit can be excited to unity, and the inner orbit may flip from prograde to retrograde or vice versa (Naoz et al. 2011; Lithwick & Naoz 2011; Katz et al. 2011; Naoz et al. 2013). As the eccentricity increases, the pericenter distance decreases and causes an enhanced tidal disruption rate (G. Li et al., in preparation). Furthermore, including the octupole effects, oscillations of the eccentricity and the inclination of the inner orbit may still exist when $i < 39°.2$, and the inner orbit may undergo a coplanar flip from ~0° to ~180° (Li et al. 2014).

Here, we probe the test particle limit, which simplifies the analysis due to its smaller number of degrees of freedom. This approximation was proven to be very useful in a large range of astrophysical settings (Lithwick & Naoz 2011; Katz et al. 2011; Naoz et al. 2012; Li et al. 2014; S. Naoz & J. Silk, in preparation; G. Li et al., in preparation). Importantly, probing this limit can help us gain some basic understanding of the EKL mechanism. The test particle limit has been studied in the literature before to obtain an analytical understanding of the flip of the orbit (Lithwick & Naoz 2011; Katz et al. 2011). Nevertheless, a systematic study of the chaotic behavior and the identification of the underlying resonances are necessary but are uncovered in the literature. We identify the resonances, and characterize the chaotic regions and the initial conditions where high eccentricity and flips may occur in the parameter space. This can help predict the dynamical evolution of systems without doing a large amount of simulations.

This paper is organized as follows. In Section 2, we give a brief overview of the Kozai–Lidov mechanism. In Section 3, we investigate the surface of section systematically for a large
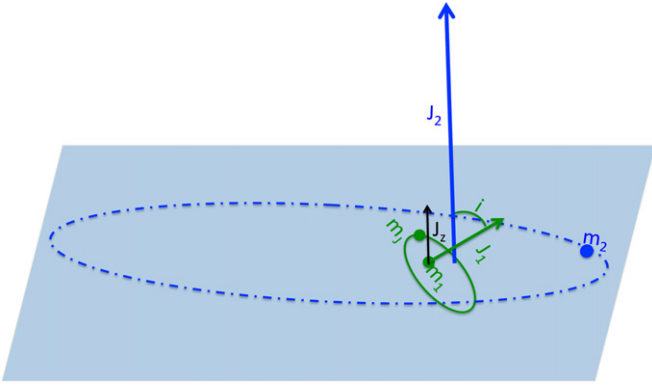
Figure 1. System configuration. A test particle m_t orbits around an object m_1 and forms the inner binary. The outer binary consists of the objects (m_2) and m_1 (in the test particle limit). J_o represents the angular momentum of the outer binary, J represents that of the inner binary, and J_z represents the $\hat{z}$ component of J, where $\hat{z}$ is in the direction of J_o. In the test particle limit, $J \ll J_o$ and the outer orbit is stationary.

(A color version of this figure is available in the online journal.)

range of orbital parameters. In Section 4, we characterize the initial condition which allows large amplitude oscillations in eccentricity and inclination. Finally, in Section 5, we characterize the chaotic regions.

2. OVERVIEW OF THE ECCENTRIC KOZAI–LIDOV MECHANISM IN THE TEST PARTICLE LIMIT

As mentioned in the introduction, the Kozai–Lidov mechanism describes the dynamical behavior of hierarchical three-body systems (see Figure 1). The inner two objects (m_1 and m_t) form an inner orbit, and the outer orbit is formed by the outer object (m_2) orbiting around the center of mass of the inner two objects. The eccentric Kozai–Lidov mechanism describes the dynamics when the outer orbit is eccentric, and the test particle limit requires one of the closely separated objects to be a test particle $m_t \rightarrow 0$.

In the hierarchical configuration, we average over the mean motion of the two orbits and treat the evolution of the system as the interaction of two elliptical wires, which is known as the secular approximation. This approximation reduces this system from six degrees of freedom to four degrees of freedom. In addition, in the test particle limit, the outer orbit is stationary and reduces the system to two degrees of freedom (Harrington 1968, 1969; Ford et al. 2000). Expanding the Hamiltonian of the interaction energy between the two ellipses in a power series of a_1/a_2, the Hamiltonian can be expressed as the following at the second (quadrupole) and third (octupole) orders (Lithwick & Naoz 2011):

$$F_{\text{quad}}(J, \omega, J_z, \Omega) = \frac{1}{2}(-1 + J^2) + \frac{J_z^2}{J^2} + \frac{3(1 - J^2)J_z^2}{2J^2} \quad (1)$$

$$+ \frac{1 - J^2}{1 - J_z^2/J^2} \cos(2\omega) F_{\text{oct}}(J, \omega, J_z, \Omega) = \frac{5}{16}\left(\sqrt{1 - J^2}\right.$$

$$+ \frac{3}{4}(1 - J^2)^{3/2}\left[\left(1 - \frac{11J_z}{J} - \frac{5J_z^2}{J^2} + \frac{15J_z^3}{J^3}\right)\cos(\omega - \Omega)\right.$$

$$+ \left(1 + \frac{11J_z}{J} - \frac{5J_z^2}{J^2} - \frac{15J_z^3}{J^3}\right)\cos(\omega + \Omega)\right]$$

$$- \frac{175}{64}(1 - J^2)^{3/2}\left[\left(1 - \frac{J_z}{J} - \frac{J_z^2}{J^2} + \frac{J_z^3}{J^3}\right)\cos(3\omega - \Omega)\right.$$

$$+ \left(1 + \frac{J_z}{J} - \frac{J_z^2}{J^2} - \frac{J_z^3}{J^3}\right)\cos(3\omega + \Omega)\right], \quad (2)$$

where $H_{\text{quad}} = -F_{\text{quad}}$ and $H_{\text{oct}} = -F_{\text{quad}} - \epsilon F_{\text{oct}}$, and

$$\epsilon = \frac{a_1}{a_2}\frac{e_2}{1 - e_2^2}. \quad (3)$$

ϵ characterizes the importance of the octupole order. The Hamiltonian is scaled with $m_t\sqrt{Gm_1a_1}t_K$, where

$$t_K = \frac{8}{3}P_{in}\frac{m_1}{m_2}\left(\frac{a_2}{a_1}\right)^3\left(1 - e_2^2\right)^{3/2} \quad (4)$$

(Lithwick & Naoz 2011). $J = \sqrt{1 - e_1^2}$ is the specific angular momentum of the inner orbit, ω is the argument of the periapsis of the inner orbit, $J_z = \sqrt{1 - e_1^2}\cos i_1$ is the $\hat{z}$ component of the inner orbit's angular momentum J, and Ω is the longitude of the ascending node of the inner orbit. Specifically, J, ω and J_z, Ω are conjugate momentum and coordinate pairs. We denote by e_1 the eccentricity of the inner orbit, and by i_1 the inclination of the inner orbit to the total angular momentum of the system. In the test particle limit, $i_1 = i$ is the mutual inclination between the two orbits.

The secular approximation breaks down when the change in the angular momentum of the inner binary happens faster than the orbital timescales (see Equation (B14) in Ivanov et al. 2005, Equation 18 in Antonini et al. 2014, and Equation (48) in Bode & Wegg 2014). Since the analysis presented here is for the reduced Hamiltonian (note that J is the specific angular momentum: $J = \sqrt{1 - e^2}$), which is independent of the masses, the timescales can be set arbitrarily and the secular approximation is irrelevant here. Nevertheless, applying this study to physical systems requires the correct scaling of the masses to satisfy the criteria for the secular approximation.

In the quadrupole limit, the Hamiltonian is independent of Ω, so J_z is constant, and the system is integrable. In addition, the angle $\omega = \varpi - \Omega$ is the resonant angle of the system, where ϖ is the longitude of the periapsis. When $i > 39°.2$, the solution admits a resonant region and e_1 and i exhibit large amplitude oscillations. Particularly, e_1 may be excited to high values starting from $e_1 \sim 0$ (e.g., Morbidelli 2002).

As mentioned in the introduction, the octupole order adds variations in J_z which allows the inner orbit to flip from prograde to retrograde, and the eccentricity to be excited very close to 1 (Lithwick & Naoz 2011; Katz et al. 2011; Naoz et al. 2011, 2012, 2013). In the following sections, we work with the Hamiltonian at the octupole level of approximation to analyze the surface of section and the chaotic behaviors.

3. SURFACES OF THE SECTION

For a two-degrees of freedom system, the surface of section projects a four-dimensional trajectory on a two-dimensional surface. Specifically, we plot points on a two-dimensional surface composed of one canonically conjugate pair (e.g., J–ω or J_z–Ω) whenever the other angle (Ω or ω) reaches a fixed value and moves in a fixed direction (see the left panel in Figure 2). The collection of points form the surface of section.

There are three distinct regions in the surface of section: "resonant regions," "circulation regions," and "chaotic regions"
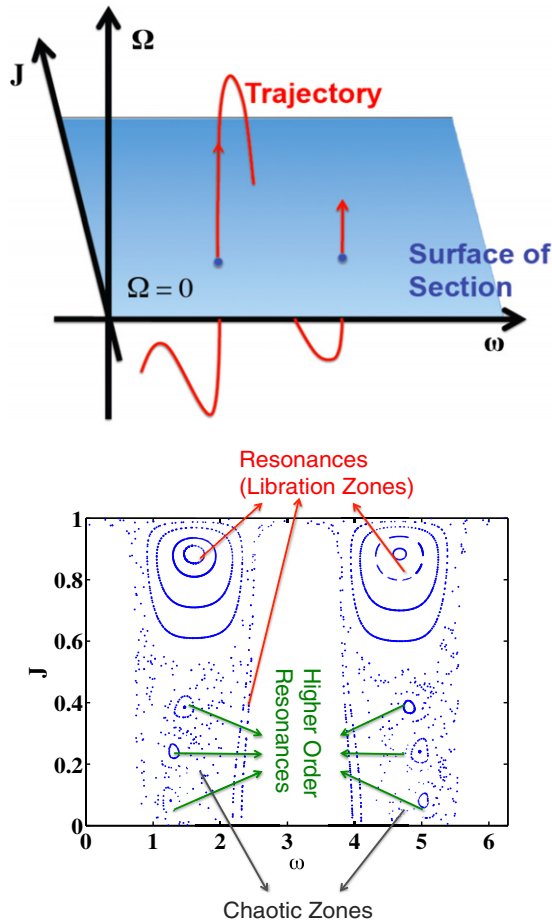
Figure 2. Upper panel: illustration of the "surface section" for the J–ω plane. By recording the point in the trajectory every time $\Omega = 0$, $\dot{\Omega} > 0$, the trajectory can be represented by a two-dimensional graph, as shown in the left panel. This set of points forms the "surface of section." Lower panel: illustration of the resonant and chaotic regions on the surface of section. We set $H = -0.1$, $\epsilon = 0.1$ in this plot. The resonant and higher-order resonant zones are marked by the red and the green arrows. The chaotic zones are indicated by the gray arrows. In the resonant region, the angle ω is constrained in a small region and the trajectories are quasi-periodic. In the chaotic region, the position of the points are not regular and the trajectories are chaotic.

(A color version of this figure is available in the online journal.)

(right panel in Figure 2). The resonant regions are formed by points where the momenta and coordinates (the angles) undergo bound oscillations. The trajectories in this region are quasi-periodic, where the system is in the *liberation* mode. The *circulation* region represents trajectories where the coordinates are not constrained to a specific interval. Both resonant and circulatory trajectories map onto a one-dimensional manifold on the surface of section. On the contrary, chaotic trajectories map onto a two-dimensional manifold. In other words, while quasi-periodic trajectories form lines on the section, chaotic trajectories are area-filling. Embedded in the chaotic region, the small islands correspond to the higher order resonances, which are caused by the interaction between the primary resonances. The trajectories in the higher order resonant regions are also quasi-periodic.

We now consider the surface of section in the J–ω plane (setting $\Omega = 0$ and $d\Omega/dt > 0$). When e_1 is excited to large values, $J \to 0$. When Ω is set, for each point in the J–ω plane, J_z ($-J \leqslant J_z \leqslant J$) is unequivocally defined by the conservation of H. There is a finite range of H that the system can take on,

because both actions must have zero imaginary components. Since we plot the sections with constant H values, we first explore the range of energy H it can achieve in the J–ω plane. This way, we can select the range in H that we explore below.

We note that the maximum and minimum energy it can reach in the J–ω plane when $\Omega = 0$ is ~ 3 and ~ -2.4 (see Appendix Figures 8 and 9, which show the maximum and the minimum H in the J–ω plane). Thus, we plot six surfaces of section for H ranging from $H = -2$ to $H = 1.2$, since when $H > 1.2$, the behavior is similar to that of $H = 1.2$. Note that the H admits positive values for this bound system, because it is the interaction energy between the test particle (m_t) and the outer companion (m_2), i.e., the disturbing function of this system to the Kepler Hamiltonian of the inner and outer orbits. To investigate the role of the octupole effects, we plot the surface section for two extreme values of ϵ: $\epsilon = 0.001$ and $\epsilon = 0.1$. When $\epsilon < 0.001$, the octupole effects are negligible. On the other hand, $\epsilon = 0.1$ represents the maximal octupole effects, where, when $\epsilon > 0.1$, the hierarchical condition may break down and the system may become unstable.

The sections are shown in Figure 3. The empty region (bounded by the black curves) do not have physical solutions. The comparison between the two rows in Figure 3 shows the difference between the octupole and the quadrupole resonances: $\epsilon = 0.001$ is dominated by the quadrupole effect and $\epsilon = 0.1$ is dominated by both the quadrupole and the octupole effects. For the former, where the quadrupole dominates, there are two resonant regions with fixed points at $\omega = \pi/2$ and $3\pi/2$ when H is high (as shown in Figure 3 at $\epsilon = 0.001$, $H = -0.5, -0.1, 0.5$ and 1.2). For the latter when the octupole plays an important role (i.e., $\epsilon = 0.1$), we find different resonant regions for different energy levels, and the location of the resonant regions varies according to the energy levels.

The resonant regions are associated with fixed points at $\omega = \pi$, $\omega = \pi/2$ and $\omega = 3\pi/2$ depending on the energy level. The resonances at high J and at $\omega = \pi/2$ or $3\pi/2$ correspond to the quadrupole resonances identified in the literature (Kozai 1962; Holman et al. 1997; Morbidelli 2002). The other resonant zones result from the interaction of the resonances associated with the "harmonics" in the octupole level Hamiltonian, i.e., 2ω, $\omega \pm \Omega$, and $3\omega \pm \Omega$. Moreover, chaotic regions can only be seen for high ϵ at $H = -0.5$ and $H = -0.1$, where reading from the surfaces, the chaotic zones are a result of the overlap of the resonances between the quadrupole and the octupole resonances (e.g., Chirikov et al. 1979; Murray et al. 1997). Embedded in the chaotic region, higher-order resonances can be found at $H = -0.1$, where the trajectories are quasi-periodic and the eccentricity cannot be excited.

On the other hand, the comparison between the different energy levels shows that the orbital evolution corresponds to different orbital parameters. The corresponding e_1 and i are shown in Figures 10 and 11 in the Appendix. Accordingly, the low H corresponds to the low inclination ($i \sim 0°$–$30°$) and high eccentricity ($e_1 \gtrsim 0.6$) case, the higher H corresponds to the high inclination ($i \sim 30°$–$60°$) and low eccentricity ($e_1 \lesssim 0.6$) case, and $H > 0$ corresponds to the high inclination ($i \sim 60°$–$90°$) and low eccentricity case ($e_1 \lesssim 0.3$). When H is low ($H \sim -2$), the evolution is only affected by the octupole resonances, while when H is higher, octupole and quadrupole resonances both contribute and may overlap to cause the chaotic region as mentioned above. We find that e_1 can be excited to high values ($J \to 0$) for almost all energy levels but is only excited very close to unity for higher ϵ. This emphasizes that
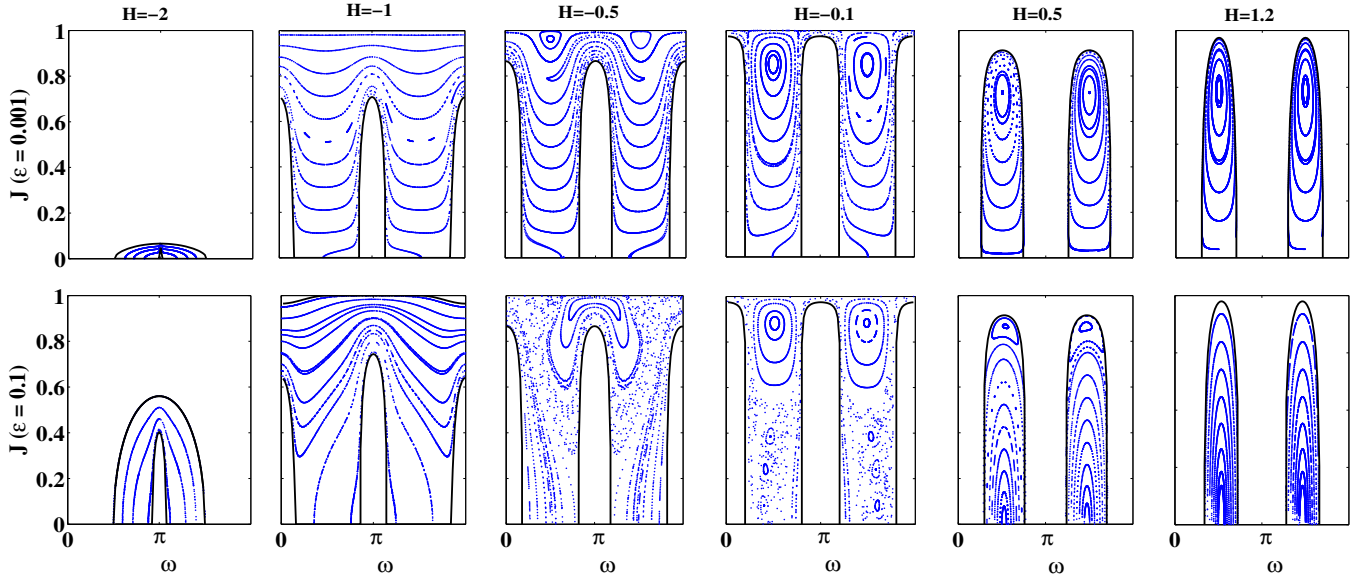
Figure 3. Surface of section in the J–ω plane. In the first row, $\epsilon = 0.001$ and in the second row, $\epsilon = 0.1$. The octupole terms are important when ϵ is bigger. H varies from $-2 \sim 1$. The corresponding e_1 and i in this plane is shown in Figures 10 and 11. There are chaotic regions at $H = -0.5$ and $H = -0.1$.

(A color version of this figure is available in the online journal.)
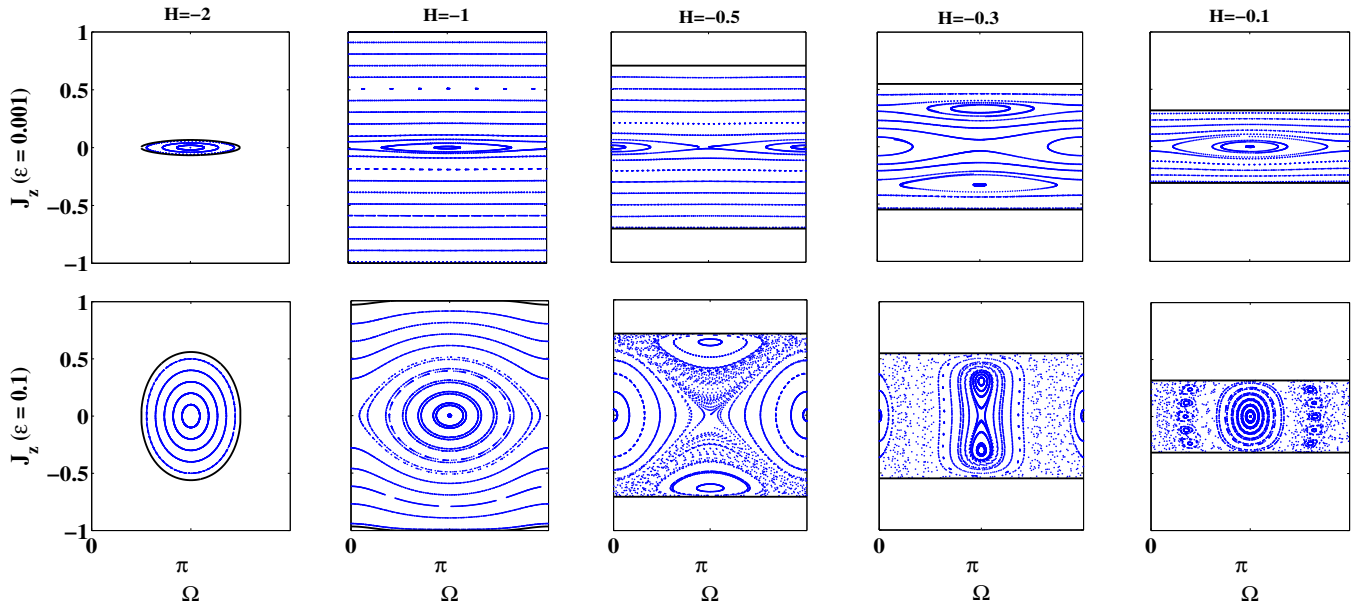
Figure 4. Surface of section in the J_z–Ω plane. In the first row, $\epsilon = 0.001$ and in the second row, $\epsilon = 0.1$. H varies from $-2 \sim 0$. There are chaotic regions at $H = -0.5$, $H = -0.3$, and $H = -0.1$. All the features are due to the octupole order, as J_z is constant in the quadrupole order. The corresponding e_1 and i are shown in Figures 12 and 13.

(A color version of this figure is available in the online journal.)

the octupole level of approximation causes large eccentricity excitation, since a larger ϵ implies that the octupole level is important.

Next, we study the surface section in the J_z–Ω plane (Figure 4). These sections clearly show the flip of the orbit when J_z changes sign. The maximum and minimum energy that can be reached in the J_z–Ω plane (with $\omega = 0$) is ~ 0 and ~ -2.4. Thus, we plot the surface of section ranging from $H = -2$ to $H = -0.1$ for two values of $\epsilon = 0.001$ and 0.1. At the quadrupole level, J_z is constant, and there are no resonances in the J_z–ω plane. Thus, all the resonances originated from the octupole level of approximation, and the fixed points are at $\Omega = \pi$ and $\Omega = 0$. In addition, similar to the surface

section on the J–Ω plane, we see higher-order resonances for $\epsilon = 0.1$ at $H = -0.3$ and $H = -0.1$ embedded in the chaotic region, and the chaotic region is confined to $H = -0.5$ and $H = -0.1$. Since J_z changes sign in all energy levels, the orbit may flip for all energy levels, and the flip parameter space is larger for higher ϵ. The corresponding e_1 and i on the surface are shown in Figures 12 and 13.

To summarize, the surfaces of section show that flips and the excitation of e_1 can occur for both regular regions and chaotic regions for a wide range of H, and they depend sensitively on the initial condition. In addition, the trajectories are chaotic only when $H \lesssim 0$, corresponding to high mutual inclination, low eccentricity cases. Furthermore, it is the octupole resonances
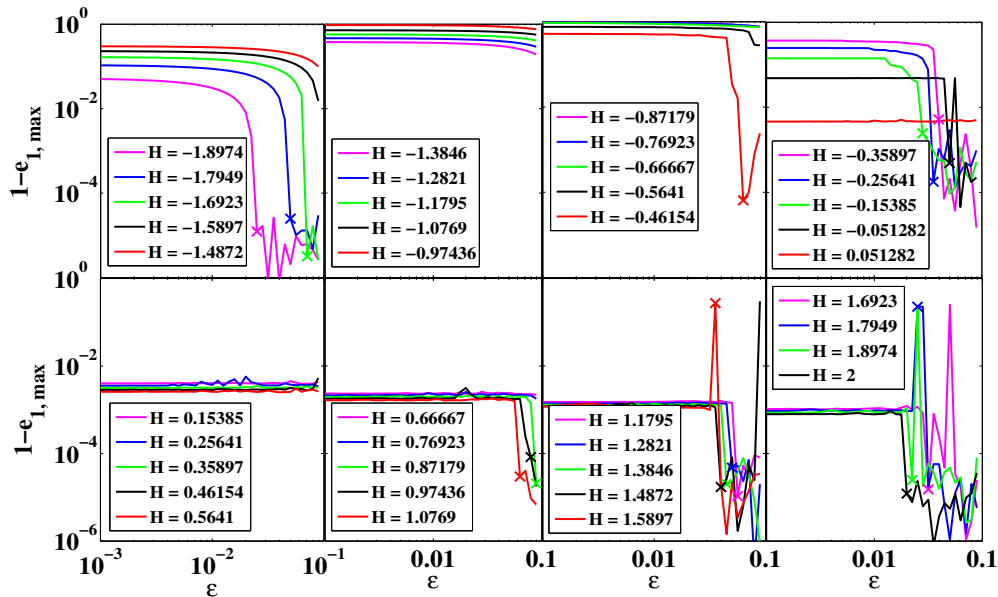
Figure 5. Maximum e_1 for different H and ϵ. We set the initial condition at the top of the energy boundary condition of the $J-\omega$ plane, and we record the maximum e_1 reached in $t = 500 t_K$. Each line represents a different H, and the cross marks the ϵ bigger than which the inner orbit may flip (i crosses over $90°$). We find that e_1 may be excited and the orbit may flip when $H \lesssim -1.5$, $-0.5 \lesssim H \lesssim 0$, and $H \gtrsim 0.5$. The first case corresponds to the coplanar flip (i flips from $\sim 0°$ to $\sim 180°$ or vice versa), and the latter two correspond to the high inclination flip.

(A color version of this figure is available in the online journal.)

that cause the flip of the orbit and the excitation of eccentricity very close to unity.

4. THE MAXIMUM ECCENTRICITY AND THE FLIP CONDITION

To apply this mechanism to astrophysical systems with different initial conditions, we investigate the parameter regions that exhibit interesting dynamical behaviors. We create a finer grid of H and ϵ than those presented in Figures 3 and 4, and we monitor the trajectories that start with the selected initial condition in the $J-\omega$ or the $J_z-\Omega$ plane. Of course, some behaviors which do not pass through the selected initial condition will be missed, but this exploration gives a general idea of the behavior of the system as a whole.

We start with the exploration in the $J-\omega$ plane. To systematically estimate the range in J that the trajectories may reach, we start at the maximum energy boundary of J for a given H and ϵ, which corresponds to the minimum eccentricity. Accordingly, for $H < -1$, ω starts at π, and for $H > -1$, ω starts at $\pi/2$. The maximum e_1 is recorded after monitoring for $t = 500 t_K$ (we define t_K in Equation (4)), which is much longer than the Lyapunov timescale (see below).

In Figure 5, we plot $1 - e_{1,\max}$ as a function of ϵ, where each curve represents a fixed H ($H \in [-2, 2]$), and ϵ ranges from 0.001 to 0.1. In addition, we use the symbol "x" to mark the ϵ higher than which the orbit flips. It shows that there are roughly five dynamical regions in H: when $H \lesssim -1.5$, $-0.5 \lesssim H \lesssim 0$, and $H \gtrsim 0.5$, the orbit may flip and e_1 can be excited very close to unity; when $-1.5 \lesssim H \lesssim -0.5$ and $0 \lesssim H \lesssim 0.5$, starting with the minimum e_1, e_1 cannot be excited to unity. Reading from the surface of section in Figure 3, the lack of e_1 excitation at $0 \lesssim H \lesssim 0.5$ and high ϵ is due to the quadrupole resonances, which traps the trajectory at low e_1.

Particularly, e_1 may be excited and the orbit may flip in three scenarios: when the inner orbit is eccentric and coplanar, when the inner orbit is circular and with high inclination, or when the

inner orbit is moderately eccentric and with very high inclination $\sim 80°$–$90°$ (see Figure 14). In addition, the maximum change in ΔJ can be well fit by a power law:

$$\Delta J = \begin{cases} e^{-2.77H-3.62}\epsilon^{0.051H+1.08} & (H < -1) \\ e^{2.14H+1.23}\epsilon^{0.75H+2.00} & (H > -1). \end{cases} \quad (5)$$

Next, we explore the $J_z-\Omega$ plane. We start the trajectories at the lower energy boundary of J_z at $\Omega = \pi$ for the given H and ϵ, and we record the maximum change in J_z after $t = 500 t_K$. Figure 6 shows ΔJ_z as a function of ϵ, where each curve represents a different H. ϵ ranges from 0.001 to 0.1, and H ranges from -2 to 0, since the maximum H is zero for $\omega = 0$. Similarly to the $J-\omega$ plane, we use the symbol "x" to mark the ϵ higher than which the orbit flips. As expected, it shows that the orbit may flip when $-2 < H < -1.5$ and $-0.5 < H < 0$, where $-2 < H < -1.5$ corresponds to an eccentric and coplanar inner orbit, and $-0.5 < H < 0$ corresponds to a circular inner orbit with a high inclination. Moreover, ΔJ_z can be fit by a power law of H and ϵ:

$$\Delta J_z = \begin{cases} e^{-2.21}\epsilon^{1.06} & (H < -0.5) \\ e^{10.7H+4.23}\epsilon^{0.48H+1.31} & (H > -0.5). \end{cases} \quad (6)$$

Note that Equations (5) and (6) are for the specific initial conditions mentioned above. They show the general dependence of the maximum change in J and J_z on ϵ and H.

5. CHAOTIC REGIONS

The surfaces of section show that the system is chaotic when $H \lesssim 0$ (Figures 3 and 4). To better characterize the chaotic regions, we first calculate the percentage of area that is chaotic in each surface in Figure 3. Specifically, we divide each surface into equally spaced grids in J and ω, and count the fraction of grids that has chaotic trajectories. We use the Lyapunov exponent
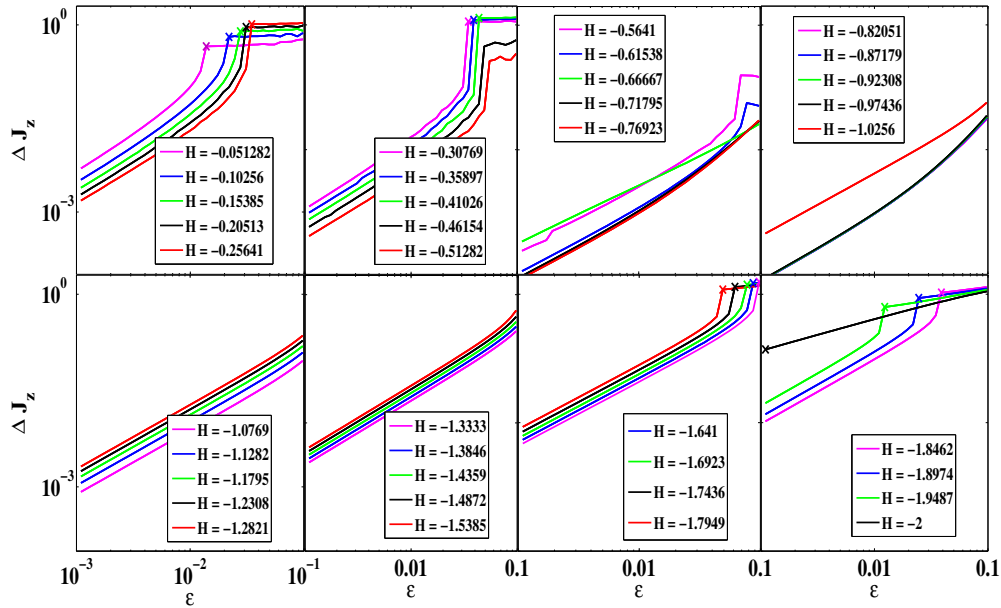
Figure 6. Maximum change in J_z for different H and ϵ. We set the initial point at $\Omega = \pi$, where J_z is on the lower energy boundary. We record the maximum change in J_z for $t = 500 t_K$. The crosses represent the ϵ bigger than which the inner orbit may flip (J_z changes sign). We find the orbit may flip at $-2 < H < -1.5$ and $-0.5 < H < 0$. The former corresponds to the coplanar flip and the latter corresponds to the high inclination flip.

(A color version of this figure is available in the online journal.)

(λ) to determine whether the trajectories are chaotic, where λ indicates how quickly two closely separated trajectories diverge from each other,

$$\lambda = \lim_{t \to \infty} \frac{1}{t} \ln \frac{\delta_{\mathrm{traj}}(t)}{\delta_{\mathrm{traj}}(0)}. \qquad (7)$$

We integrate the tangent of the trajectories for $1000 t_K$ to compute λ, and we find that there are chaotic trajectories only when $\epsilon = 0.1$, $H = -0.5$ or -0.1. Specifically, 85 out of 276 ($\sim 31\%$) grid cells have chaotic trajectories when $\epsilon = 0.1$ and $H = -0.5$, and 109 out of 242 ($\sim 45\%$) grid cells have chaotic trajectories when $\epsilon = 0.1$ and $H = -0.1$. It shows that even when $H \lesssim 0$, a large range of orbital parameters would still yield regular trajectories.

Next, we characterize the chaotic region in the parameter space of H and ϵ. We arbitrarily select the trajectories starting with $\Omega = 0$, $\omega = \pi/2$, and the maximum J for the given H and ϵ, where the associated e_1 and i of the initial condition are shown in Figure 14. Similarly, we integrate the tangent of the trajectories for $1000 t_K$ to compute λ, and we plot λ as a function of H and ϵ in the left panel of Figure 7. The larger λ corresponds to the more chaotic systems. A large region in the parameter space is regular, and the system is chaotic only when $-0.6 < H < 0$ for larger ϵ. The Lyapunov timescale is $\sim 6 t_K$ when $\epsilon \gtrsim 0.01$ and $-0.6 < H < 0$ (low e_1 and $i \gtrsim 40°$).

To justify that the regions with smaller λ are regular, we increase the run time to $4000 t_K$, and we find that the Lyapunov exponents for the regular region decrease, while the Lyapunov exponents in the chaotic region remain at $\sim 6 t_K$. Moreover, to avoid missing chaotic regions due to the specific choice of the initial condition, we vary the initial condition and make several contour plots of λ in the plane of H and ϵ. The right panel of Figure 7 shows the case when ω starts at 0, where the trajectories are also chaotic when $-0.6 < H < 0$.
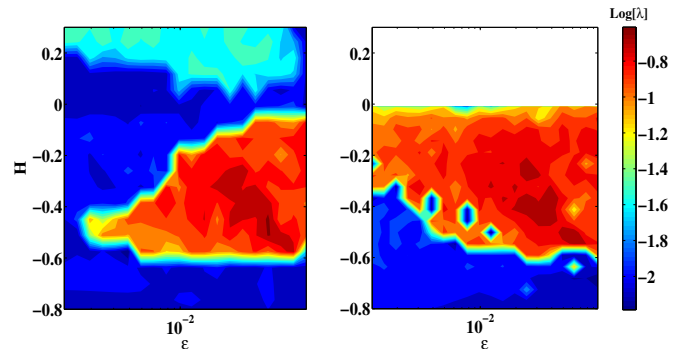

Figure 7. Lyapunov exponents with different H and ϵ. Run time $t = 1000$. Left panel: we consider the following initial condition: $\omega_0 = \pi/2$, $\Omega_0 = 0$, $J_0 = 1$, or the maximum J at the energy boundary and $-0.8 < H < 0.3$. Right panel: we consider the following initial condition: $\omega_0 = \Omega_0 = 0$, $J_0 = 1$, and $-0.6 < H < 0$. Note that for this choice of initial conditions no physical solution exists for $H > 0$. The colormap represents the value of the Lyapunov exponents λ. The yellow and red colors correspond to large Lyapunov exponents, which are associated with chaotic regions, and the cyan and blue colors represent the regular regions.

(A color version of this figure is available in the online journal.)

6. CONCLUSION

The hierarchical three-body system in the test particle limit is common in a large range of astrophysical settings. The dynamical behavior of such systems may lead to retrograde objects, an enhanced rate for tidal disruption, and merger or collision events (e.g., Holman et al. 1997; Fabrycky & Tremaine 2007; Naoz et al. 2011, 2012; Chen et al. 2011; Bode & Wegg 2013; S. Naoz & Silk, in preparation; G. Li et al., in preparation). Here, we used a large range of the initial condition to systematically study the dynamics, including the underlying resonances, and the chaotic characteristics of the system.

First, we plotted the surface of section on the J–ω plane for a large range of energy H and two different ϵ to identify
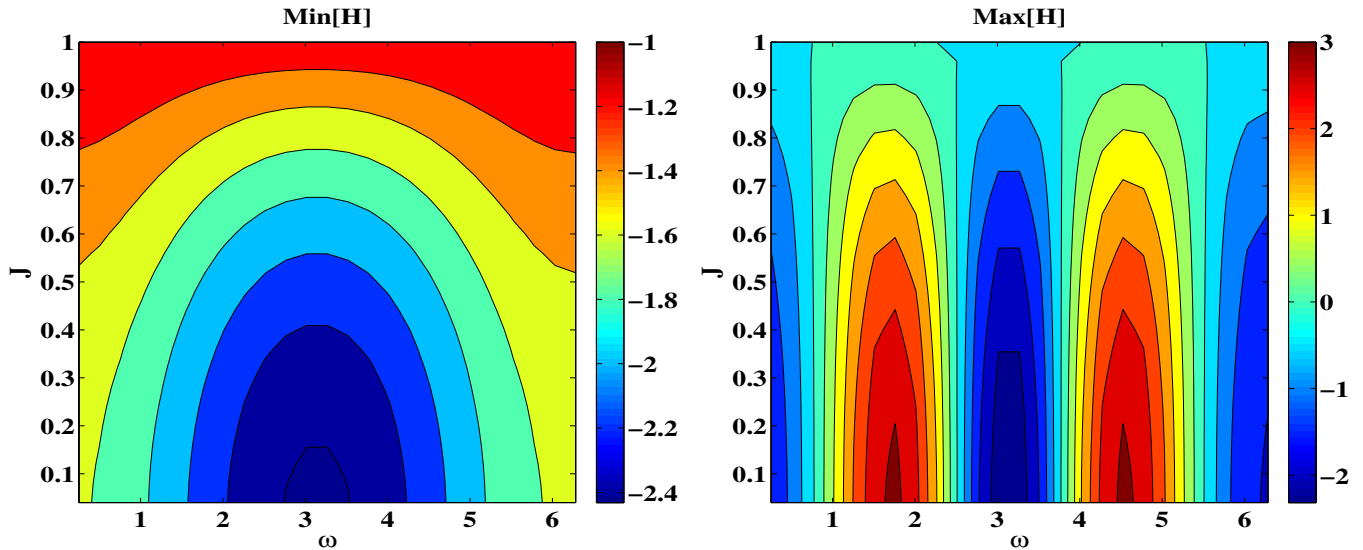
Figure 8. Maximum and minimum that H can reach for different $J - \omega$ with $\Omega = 0$. In this plot, we set $\epsilon = 0.1$. The energy range is about $-2.5 \sim 3$ in the $J-\omega$ plane. In addition, this explains the shape of the empty region (where there are no solutions) in the surface of section plot.

(A color version of this figure is available in the online journal.)
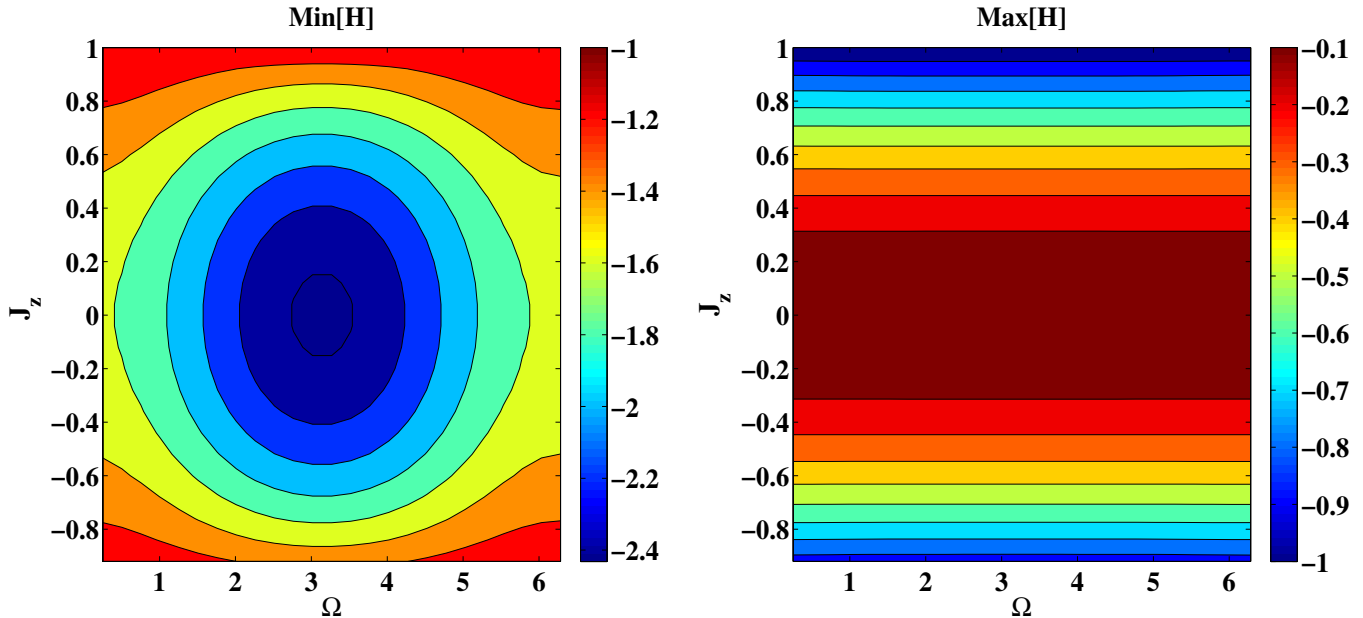
Figure 9. Maximum and minimum that H can reach for different $J_z - \Omega$ with $\omega = 0$. In this plot, we set $\epsilon = 0.1$. The energy range is about $-2.5 \sim 0$ in the $J_z-\Omega$ plane. In addition, this explains the shape of the empty region (where there are no solutions) in the surface of section plot.

(A color version of this figure is available in the online journal.)

the underlying resonances (Figure 3). In the quadrupole level, the resonances that occur at high H are centered around fixed points at $\omega = \pi/2$ and $3\pi/2$. On the other hand, the octupole level resonances are centered at $\omega = 0$, $\pi/2$, π, or $3\pi/2$ depending on the different energy levels, and we can identify resonances in all these energy levels. The octupole resonances cause the excitation of e_1 in the high eccentricity coplanar case (corresponding to low H), shown in Li et al. (2014). The overlap of the quadrupole and octupole resonances causes the chaos for the low eccentricity and high inclination case (corresponds to higher H; e.g., Naoz et al. 2011).

The surfaces of section in the $J_z-\Omega$ plane not only show the octupole resonances but the condition when the orbit flips as J_z changes sign (Figure 4). At the quadrupole level, J_z is constant,

and there is no resonant zones in the $J_z-\Omega$ plane. However, at the octupole level, the resonant zones exist and lead to the flip of the orbit. As expected, similarly to the $J-\omega$ plane, it also shows that chaotic behavior exist when $H \lesssim 0$ for high ϵ.

Finally, we calculated the Lyapunov exponent for different H and ϵ to characterize the region where the evolution is chaotic. Consistently with the surface of section, we have found that the orbital evolution is chaotic when $H \lesssim 0$ (low e_1 high i cases). Specifically, the Lyapunov timescale $\sim 6t_K$.

By monitoring the trajectories, we find that the inner eccentricity may be excited and the orbit may flip for a circular high inclination orbit or for an eccentric and nearly coplanar orbit. This agrees with previous discussions in the literature for the flips with high inclination (Naoz et al. 2011; Lithwick & Naoz
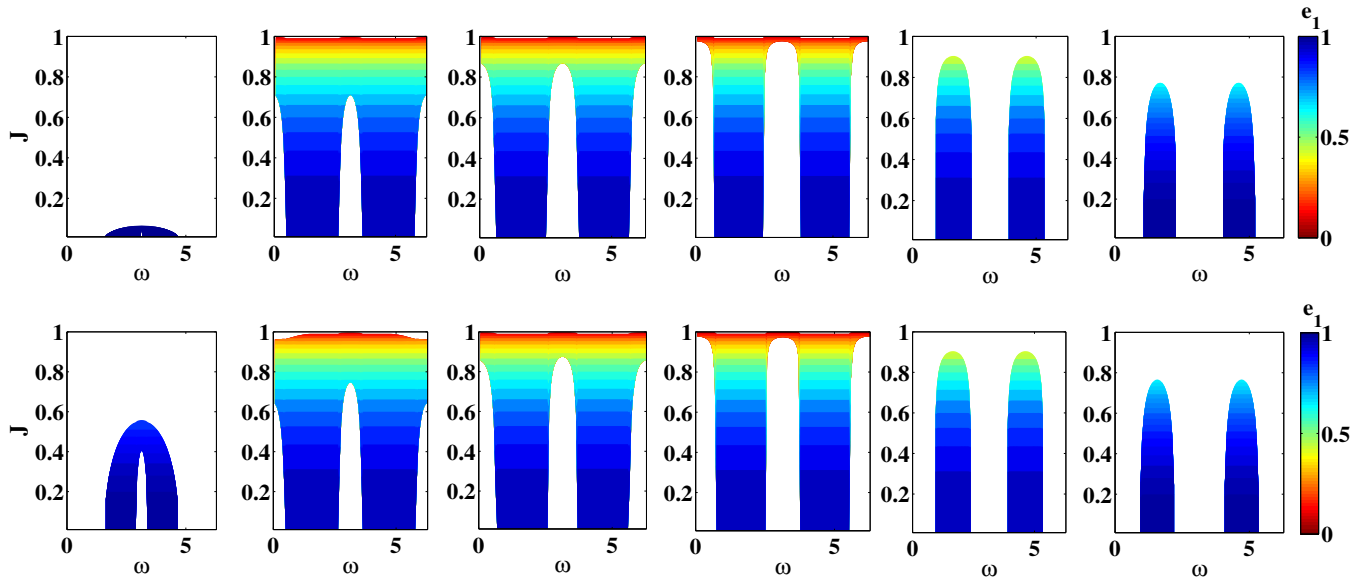
Figure 10. Eccentricities in the J–ω plane ($\Omega = 0$). Note that these are not the initial conditions, but directly the values of e_1 in the J–ω surface at fixed $\Omega = 0$ for the given H and ϵ. Similar to Figure 3, in the first row, $\epsilon = 0.001$ and in the second row, $\epsilon = 0.1$. The octupole terms are more dominant when ϵ is bigger.

(A color version of this figure is available in the online journal.)
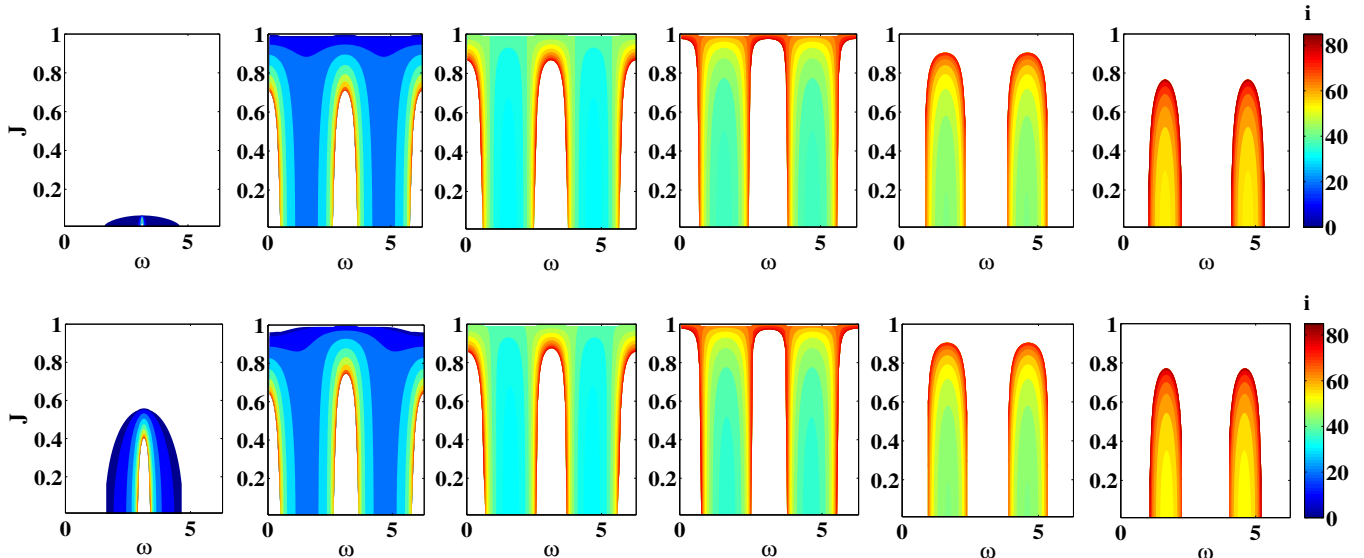
Figure 11. Inclinations in the J–ω plane ($\Omega = 0$). Note that these are not the initial conditions, but directly the values of i in the J–ω surface at fixed $\Omega = 0$ for the given H and ϵ. Similar to Figure 3, in the first row, $\epsilon = 0.001$ and in the second row, $\epsilon = 0.1$. The octupole terms are more dominant when ϵ is bigger.

(A color version of this figure is available in the online journal.)

2011; Katz et al. 2011) and coplanar flips (Li et al. 2014). In addition, we note that the flips with high inclination are chaotic and the coplanar flips are regular. This analysis can be applied to observed systems. Knowing roughly the orbital elements, one can identify the type of trajectories in the surface of section. Then, one can study the evolution features of the system without doing a large number of simulation for different initial conditions. Moreover, our analysis could help predict the enhancement in the rate of tidal disruption events due to eccentricity excitation (G. Li et al., in preparation).

APPENDIX

First, we explore the range H can reach for the surface of section in the J–ω plane with $\Omega = 0$ and in the J_z–Ω plane with $\omega = 0$. We contour plot the maximum and minimum of H as a function of J and ω while setting $\Omega = 0$ in Figure 8, which depicts that the range of H is ~-2.4 to ~3. Similarly, we plot the maximum and minimum of H for different J_z and Ω with $\omega = 0$ in Figure 9. It shows that H ranges from ~-2.4 to 0. Accordingly, we plot the surface of section for $-2 < H < 1.2$ in Figure 3, since when $H > 1.2$ the section are similar to that when $H = \sim1.2$, and we set $-2 < H < 0$ for the surface of section in Figure 4.
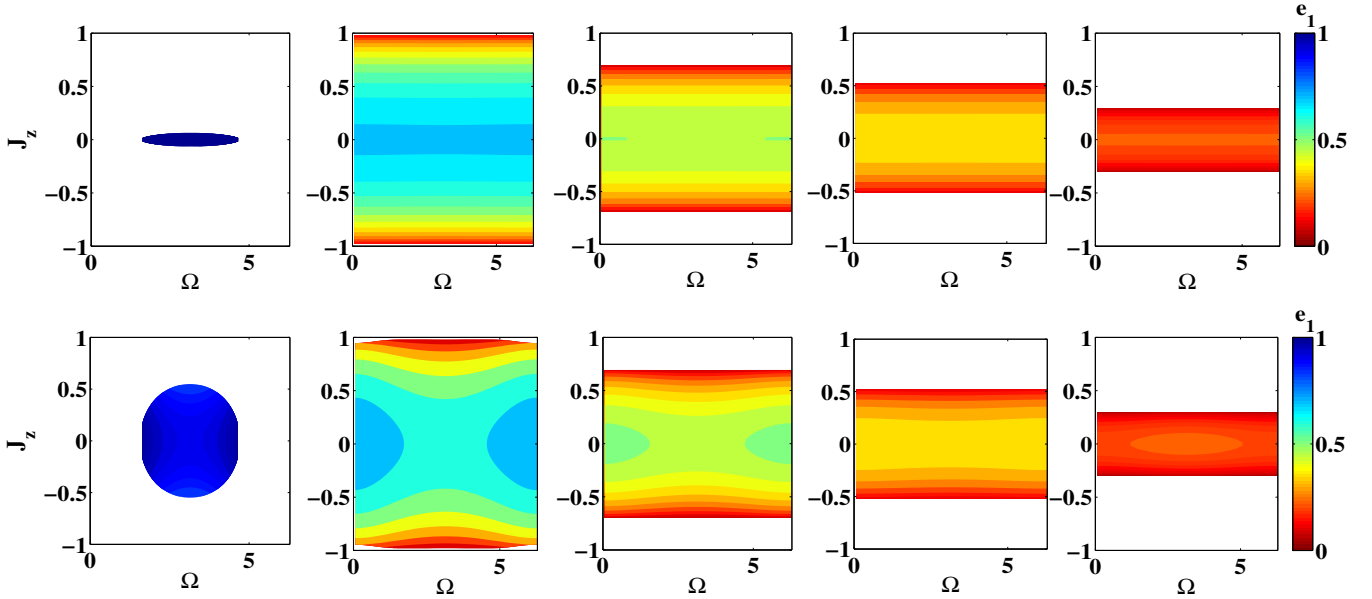
Figure 12. Eccentricities on the J_z–Ω plane ($\omega = 0$). Note that these are not the initial conditions, but directly the values of e_1 in the J_z–Ω surface at fixed $\omega = 0$ for the given H and ϵ. Similar to Figure 4, in the first row, $\epsilon = 0.001$ and in the second row, $\epsilon = 0.1$. The octupole terms are more dominant when ϵ is bigger.

(A color version of this figure is available in the online journal.)
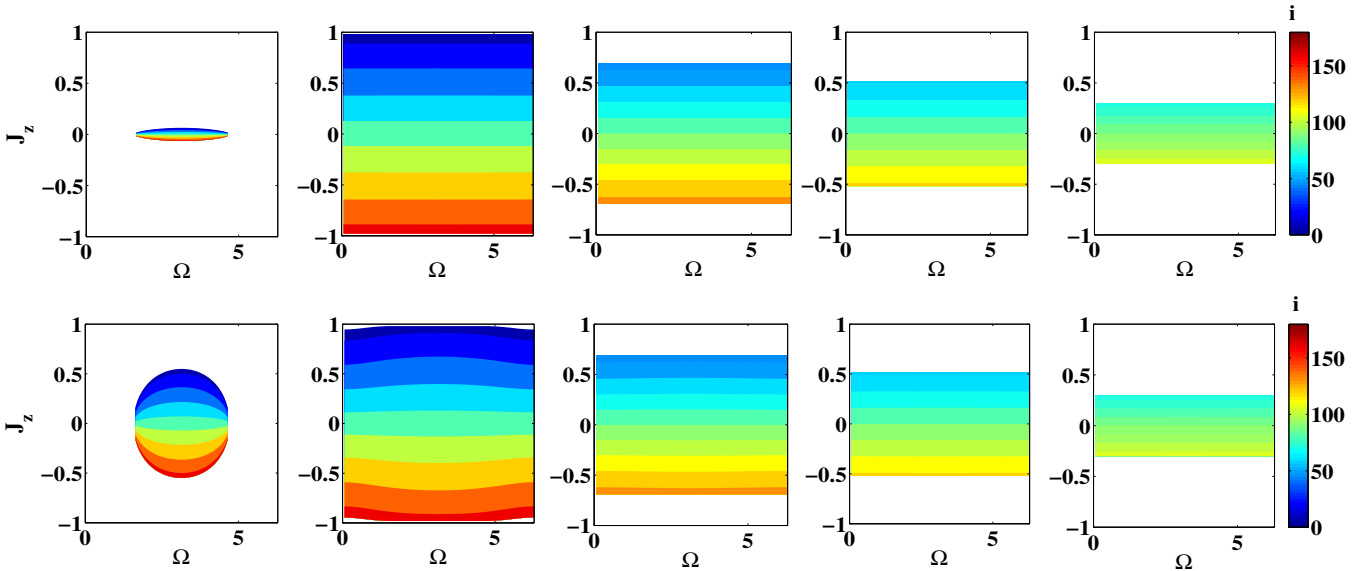
Figure 13. Inclinations in the J_z–Ω plane ($\omega = 0$). Note that these are not the initial conditions, but directly the values of i in the J_z–Ω surface at fixed $\omega = 0$ for the given H and ϵ. Similar to Figure 4, in the first row, $\epsilon = 0.001$ and in the second row, $\epsilon = 0.1$. The octupole terms are more dominant when ϵ is bigger.

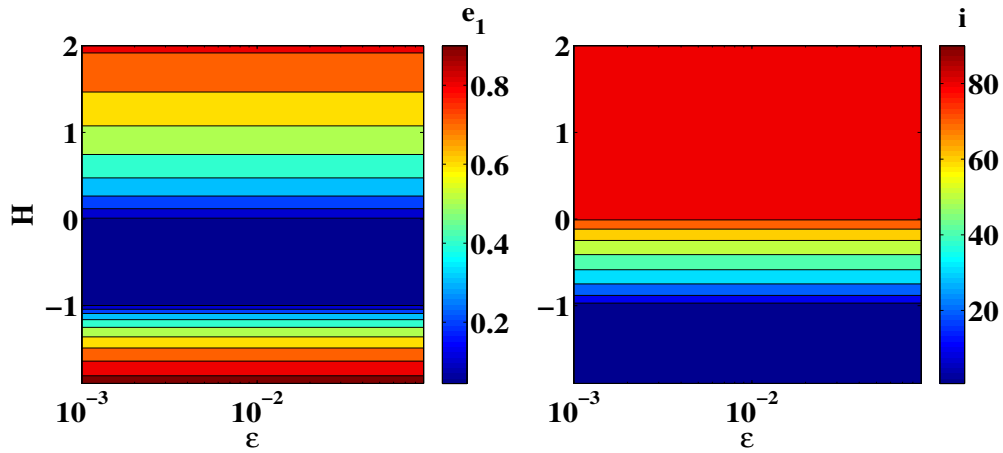(A color version of this figure is available in the online journal.)

Next, we show the associated eccentricity and inclination for the surface of section (Figures 3 and 4) and the initial condition in Figures 5 and 6. This helps to connect the resulting dynamical behavior to the parameters in e_1 and i, which can be obtained more directly for observations.

In Figures 10 and 11, we plot the initial condition in the J–ω plane corresponding to the surfaces of section in Figure 3. e_1 can be calculated from the J value directly as $e_1 = \sqrt{1 - J^2}$, so a higher J is associated with lower e_1. On the other hand, i is lower for larger J when $H = -2, -1, -0.5$, and i is higher for larger J when $H = -0.1, 0.5, 1.2$.

Next, in Figures 12 and 13, we plot e_1 and i in the J_z–Ω plane, corresponding to the surface section in the J_z–Ω plane

with $\omega = 0$ in Figure 4. When $i > 90°$, $J_z > 0$, and when $i < 90°$, $J_z < 0$. We find that e_1 is higher for lower H, and i is closer to $90°$ for higher H.

Furthermore, we plot the initial condition for the trajectories we selected to investigate the maximum e_1 in Figure 14. It shows that for the maximum e_1 plot (Figure 5), when $H \lesssim -1.2$, we monitor the trajectories that start with high eccentricity and low inclination. In this case, when $H \lesssim -1.7$, the orbit may flip at high ϵ and the maximum e_1 may reach ~ 1–10^{-6} for high ϵ. When $-1.2 \lesssim H \lesssim 0$, we monitor trajectories that start with low eccentricity and high inclination. In this case, not much variation is seen unless $H \lesssim 0$. When $H > 0$, we monitor trajectories starting with high inclination $i \sim 80°$–$90°$.

Figure 14. e_1 and i with $\omega_0 = \pi$ ($H < -1$), $\omega_0 = \pi/2$ ($H > -1$), $\Omega = 0$, and J at the upper energy boundary. This is associated with the initial condition for Figure 5, i.e., the initial e_1 and i_1 for each run at fixed ϵ and H.

(A color version of this figure is available in the online journal.)
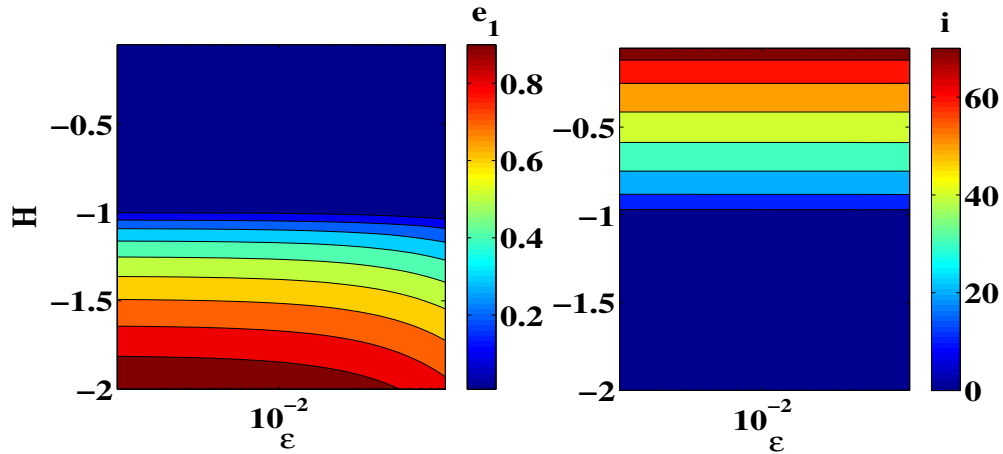
Figure 15. e_1 and i_1 with $\Omega = \pi$, $\omega = 0$, and J_z are at the lower energy boundary for different H and ϵ. This is associated with the initial condition in Figure 6, i.e., the initial e_1 and i_1 for each run at fixed ϵ and H.

(A color version of this figure is available in the online journal.)

In the end, we plot the initial condition for the trajectories that are monitored for J_z or the flip of the orbit in Figure 15. When $H \lesssim -1$, we start the trajectories with high e_1 and low i; when $H \gtrsim -1$, we start the trajectories with low e_1 and high i. The orbit may flip with $-0.4 \lesssim H \lesssim 0$ at high ϵ for trajectories starting with low e_1 and high i, and the orbit may flip with $H \lesssim -1.5$ when the trajectories start with high e_1 and low i.

REFERENCES

Antonini, F., Murray, N., & Mikkola, S. 2014, ApJ, 781, 45
Blaes, O., Lee, M. H., & Socrates, A. 2002, ApJ, 578, 775
Bode, J. N., & Wegg, C. 2014, MNRAS, 438, 573
Bode, N., & Wegg, C. 2013, arXiv:1310.5745
Chen, X., Madau, P., Sesana, A., & Liu, F. K. 2009, ApJL, 697, L149
Chen, X., Sesana, A., Madau, P., & Liu, F. K. 2011, ApJ, 729, 13
Chirikov, B. V. 1979, PhR, 52, 263
Correia, A. C. M., Laskar, J., Farago, F., & Boué, G. 2011, CeMDA, 111, 105
Eggleton, P. P., & Kiseleva-Eggleton, L. 2001, ApJ, 562, 1012
Fabrycky, D., & Tremaine, S. 2007, ApJ, 669, 1298
Ford, E. B., Kozinsky, B., & Rasio, F. A. 2000, ApJ, 535, 385
Harrington, R. S. 1968, AJ, 73, 190
Harrington, R. S. 1969, CeMec, 1, 200
Holman, M., Touma, J., & Tremaine, S. 1997, Natur, 386, 254
Ivanov, P. B., Polnarev, A. G., & Saha, P. 2005, MNRAS, 358, 1361
Ivanova, N., Chaichenets, S., Fregeau, J., et al. 2010, ApJ, 717, 948
Katz, B., & Dong, S. 2012, arXiv:1211.4584
Katz, B., Dong, S., & Malhotra, R. 2011, PhRvL, 107, 181101
Kiseleva, L. G., Eggleton, P. P., & Mikkola, S. 1998, MNRAS, 300, 292
Kozai, Y. 1962, AJ, 67, 591
Li, G., Naoz, S., Kocsis, B., & Loeb, A. 2014, ApJ, 785, 116
Lidov, M. L. 1962, P&SS, 9, 719
Lithwick, Y., & Naoz, S. 2011, ApJ, 742, 94
Mazeh, T., & Shaham, J. 1979, A&A, 77, 145
Miller, M. C., & Hamilton, D. P. 2002, ApJ, 576, 894
Morbidelli, A. 2002, Modern Celestial Mechanics: Aspects of Solar System Dynamics (London: Taylor & Francis)
Murray, N., & Holman, M. 1997, AJ, 114, 1246
Naoz, S., & Fabrycky, D. C. 2014, ApJ, submitted (arXiv:1405.5223)
Naoz, S., Farr, W. M., Lithwick, Y., Rasio, F. A., & Teyssandier, J. 2011, Natur, 473, 187
Naoz, S., Farr, W. M., Lithwick, Y., Rasio, F. A., & Teyssandier, J. 2013, MNRAS, 431, 2155
Naoz, S., Farr, W. M., & Rasio, F. A. 2012, ApJL, 754, L36
Perets, H. B., & Fabrycky, D. C. 2009, ApJ, 697, 1048
Shappee, B. J., & Thompson, T. A. 2013, ApJ, 766, 64
Soderhjelm, S. 1982, A&A, 107, 54
Thompson, T. A. 2011, ApJ, 741, 82
Veras, D., & Ford, E. B. 2010, ApJ, 715, 803
Wegg, C., & Bode, N. 2011, ApJL, 738, L8
Wen, L. 2003, ApJ, 598, 419
Wu, Y., & Murray, N. 2003, ApJ, 589, 605